



Revealing the Impact of Different Iron-Based Precursors on the 'Catalytic' Graphitization for Synthesis of Anode Materials for Lithium Ion Batteries

Lars Frankenstein,^[a] Pascal Glomb,^[a] Joaquin Ramirez-Rico,^[b] Martin Winter,^[a, c] Tobias Placke,^{*[a]} and Aurora Gomez-Martin^{*[a]}

Low cost and environmentally friendly production of graphite anodes from naturally available biomass resources is of great importance to satisfy the increasing material demand for lithium ion batteries. Herein, graphitization of coffee ground was performed using four different iron-based activating additives, including iron (III) chloride, iron (III) nitrate, iron (III) oxide and pure iron, following either a wet or a dry mixing approach. The structural development regarding the type of activator used and the impact on the corresponding electro-

chemical performance are systematically investigated. A maximum degree of graphitization between 55 and 74% (as determined by Raman spectroscopy) is attained using iron (III) chloride and iron powder, respectively. The graphitic anode material synthesized using iron powder reached a maximum reversible capacity of $\approx 320 \text{ mAh g}^{-1}$ at a rate of 0.1 C. This study provides significant insights into the impact of activators on the design of synthetic graphite from renewable sources.

Introduction

Since their first commercialization in the early 90 s, the demand for lithium ion batteries (LIBs) for electronic devices as well as electro mobility applications has increased steeply.^[1] LIBs are considered as a key technology to decarbonize global transport and energy sectors.^[1–2] Increasing consumer demands as well as recent concerns about process sustainability and shortages in material supply chains drive the development of advanced LIB active materials.^[3] Graphite is the state-of-the-art anode active material for LIBs due its moderate gravimetric capacity (372 mAh g^{-1} , LiC_6 stoichiometry), long cycle life, low average (de-)lithiation potential ($\approx 0.2 \text{ V}$ vs. $\text{Li} | \text{Li}^+$) and a low voltage hysteresis which results in high voltage and energy efficiencies.^[3–4] Despite silicon (Si) holds great promise as anode


active material for future high-energy density LIBs,^[5] its use in high proportions ($\geq 10\text{--}20 \text{ wt}\%$) in commercial cells is still hampered by several challenges limiting cycle life.^[6] Blending of Si with graphite particles is considered one of the most promising approaches to improve cycle life of future Si-based LIB full-cells.^[7] Therefore, it is expected that graphite will remain a mandatory material for LIB anodes in the coming years.


The demand for graphite is expected to experience an exponential growth over the coming years driven by the development of electric vehicles (EVs).^[1b,8] Two types of graphite anode materials are typically used in commercial LIB cells, i.e., natural graphite (NG) and synthetic/artificial graphite (SG).^[1b,8a] SG shows outstandingly high levels of purity and less fluctuating quality and characteristics, while NG exhibits lower costs. Therefore, the production of mixtures of SG and NG offers a good compromise between cost, energy and power densities and lifetime.^[9] However, there are raising environmental and supply bottlenecks concerns for the production of both graphite types.^[10] Currently, most of the global supply of NG and SG comes from China.^[9,11] On the one hand, SG is produced from soft carbon (i.e., 'graphitizable' carbon) precursors such as petroleum coke, which is a non-sustainable waste by-product from the oil refinery industry but can be graphitized when heat-treated at high temperatures.^[1b,12] The processing of SG comprises first carbonization step up to $800\text{--}1200^\circ\text{C}$, a second heat-treatment up to temperatures higher than 2500°C for several days up to weeks and intermediate and final particle size refinement steps.^[1b,13] Overall, the production of SG is expensive, energy-intensive, and environmentally harmful. On the other hand, NG has been classified as critical for Europe and the U.S. in terms of economic importance and supply risk due to extraction from graphite ores mainly present in China.^[12a,14] Besides NG reserves are limited, the purification of NG has severe negative impacts on the environment, such as air and

[a] L. Frankenstein, P. Glomb, Prof. Dr. M. Winter, Dr. T. Placke, Dr. A. Gomez-Martin
University of Münster
MEET Battery Research Center, Institute of Physical Chemistry
Corrensstr. 46, 48149 Münster, Germany
E-mail: agomezma@uni-muenster.de
tobias.placke@uni-muenster.de

[b] Prof. J. Ramirez-Rico
Dpto. Física de la Materia Condensada and Instituto de Ciencia de Materiales de Sevilla, Universidad de Sevilla,
Consejo Superior de Investigaciones Científicas
Avda. Américo Vespucio 49, 41092 Sevilla, Spain

[c] Prof. Dr. M. Winter
Helmholtz Institute Münster, IEK-12
Forschungszentrum Jülich GmbH
Corrensstr. 46, 48149 Münster, Germany

 Supporting information for this article is available on the WWW under <https://doi.org/10.1002/celec.202201073>

 © 2023 The Authors. ChemElectroChem published by Wiley-VCH GmbH. This is an open access article under the terms of the Creative Commons Attribution License, which permits use, distribution and reproduction in any medium, provided the original work is properly cited.

water pollution.^[10] Therefore, further attention should be paid to the search of more sustainable processing of SG.

The conversion of industrial waste by-products and naturally available biomass resources into valuable carbon materials for energy storage devices, i.e., LIBs, sodium ion batteries (SIBs) and supercapacitors, has been the subject of extensive research efforts recently.^[15] The physicochemical properties of carbon materials (i.e., degree of graphitization (DoG), particle morphology, surface area, etc.) can be easily tailored to the final application.^[16] Carbons obtained by heat-treatment of biomass resources are typically classified as 'non-graphitizable' or 'hard carbons' due to the strong cross-linking and random orientation between crystallites which precludes the development of a highly graphitic structure upon further heat-treatment.^[17] While hard carbons are preferred as anode materials in SIBs as a result of the less favoured intercalation of Na⁺ into graphite compared to that of Li⁺,^[16b,18] graphitic carbons are desirable for LIBs.

An effective approach to accelerate the development of ordered graphitic domains in hard carbons while reducing cost and energy consumption is the so-called 'catalytic' graphitization.^[19] This process involves the wet or dry addition of transition metals (Fe, Co, Ni, etc.) acting as "activators" to the carbon precursor that, upon heating, can induce the precipitation of ordered carbon regions and thus a decrease in the activation energy for crystallization.^[19a,d,20] Among transition metals, iron (Fe) is regarded as the most effective activator due to the number of free electron vacancies in the d-shell orbitals and thus the possibility to form strong covalent bonds between metal and carbon atoms.^[19b,21] According to previous studies on the graphitization of biomass, activator concentration^[22] and carbonization temperature^[22-23] play a critical role in the DoG and the electrochemical performance as anode materials in LIB cells.^[19a,22a] Gomez-Martin et al.^[19a] showed an enhanced DoG with increased heat treatment temperatures (850–2000 °C) when using an iron-based activator (iron (III) chloride) at a fixed concentration and observed improved specific capacities of the produced carbons. More recently, Hanhart et al. found an almost linear trend in achievable reversible capacities when increasing the activator content (iron (III) chloride) as well as graphitization temperature due to the increasing structural order within the carbon materials.^[22a] However, our latest study also reported that the volatility of the iron (III) chloride precursor might drive continuous evaporation from the carbon precursor causing a saturation point in the maximum DoG ($\approx 69\%$) and reversible capacity ($\approx 235 \text{ mAh g}^{-1}$) achievable.^[24] Hoekstra et al. investigated the graphitization of cellulose with different iron salts and found a worse graphitization efficiency for iron (III) chloride. From those findings, it was pointed out that the extent of graphitization might strongly depend on the iron particle size and iron salt.^[24] Banek et al. reported the conversion of hardwood sawdust to highly crystalline graphite flakes by laser pyrolysis using iron powder with similar maximum reversible capacities as known for commercial SG.^[25] Therefore, further studies investigating the effect of different iron-based precursors are needed for further tailoring and

optimization of the synthesis of more sustainable SG anodes for LIBs using biomass resources.

In this work, a detailed study of the effect of different iron-based precursors on the graphitization of coffee grounds as biomass precursor is presented. High temperature graphitization was performed at 2000 °C with four different iron-based precursors. Raman spectroscopy and total scattering X-ray diffraction experiments along with their pair distribution functions were performed to monitor the extent of graphitization in coffee-ground derived carbons. Finally, all graphitized carbon materials were electrochemically evaluated in carbon||Li metal cells and the results are discussed in connection with their DoG, crystallite size and particle morphology. This study can pave the way for further tailoring the synthesis of graphitic materials from biomass resources.

Results and discussion

Synthesis procedure and morphology of the samples

The graphitization of coffee ground was investigated using the same Fe:C mass ratio (1:1) and four different iron-based precursors, including iron (III) chloride (FeCl₃·6H₂O further referred to as 'FeCl₃-sample'), iron (III) nitrate (Fe(NO₃)₃·9H₂O abbreviated as 'Fe(NO₃)₃-sample'), iron oxide (Fe₂O₃) and pure iron (Fe). In Germany, more than 97,000 t of raw coffee is imported monthly resulting in a lot of waste given as coffee ground, leading to a possible sustainable graphite source when performing 'catalytic' graphitization.^[26] As illustrated in Figure 1, two different approaches were considered for incorporation of the iron-based activator. For the first approach, FeCl₃ and Fe(NO₃)₃ were dissolved in acetone and wet-mixed with coffee grounds. For the second approach, the biomass precursor and Fe₂O₃ or Fe as activators were mechanically mixed. These mixtures were first carbonized up to 1000 °C in an inert atmosphere to drive the thermal decomposition of the organic matter to amorphous carbon followed by a second heat-treatment at 2000 °C to promote graphitization. According to thermogravimetric analysis performed by Hanhart et al., the carbon yield from the coffee grounds carbonization can be estimated to be $\approx 20 \text{ wt}\%$ based on dry biomass weight, which seems to be low compared to other biomasses such as lignin.^[22a,27] However, coffee ground is a waste product that one should take advantage of and modifications in the carbonization step could result in higher carbon yields.^[28]

The iron content after carbonization at 1000 °C as well as after graphitization at 2000 °C and acid washing was determined by inductively coupled plasma-optical emission spectrometry (ICP-OES). Results are listed in Table S1 for all samples. Despite the same initial Fe:C ratio (1:1), the total iron content slightly differs between samples. Values between ≈ 18 and 27% were achieved. The sample containing FeCl₃ showed the lowest iron proportion most likely due to dehydration and decomposition of the iron salt at temperatures > 100 °C, in agreement with previous studies.^[22a] It has to be noted that the high amount of residual Fe for the Fe(NO₃)₃-treated sample might be

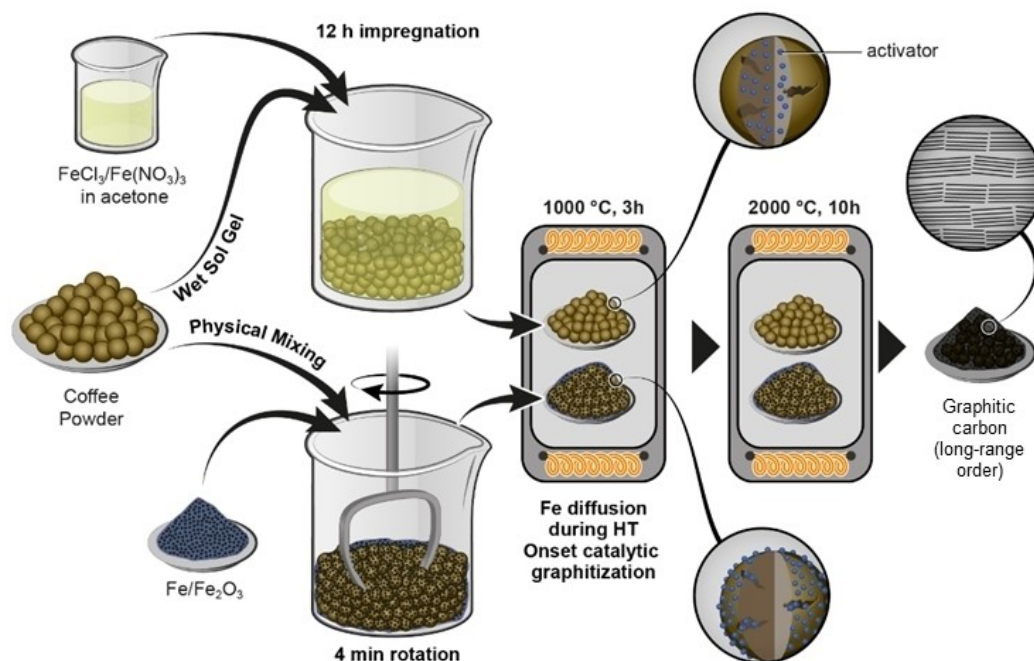


Figure 1. Graphical illustration of the synthesis conditions investigated in this work. Coffee ground was used as biomass-precursor. The activator was introduced either following a wet sol gel approach using iron (III) chloride or iron (III) nitrate in acetone or following a dry mixing approach using iron (III) oxide or iron powders. For further details, please check the experimental section.

explained by the possible lower yield of carbon during carbonization, as $\text{Fe}(\text{NO}_3)_3$ is highly oxidative. After graphitization at 2000 °C and acid washing, the residual iron content drastically fell below 1 wt%, leading to almost impurity-free graphitic carbon samples.

Representative scanning electron microscopy (SEM) images of all samples graphitized at 2000 °C shown in Figure 2 reveal significant morphological changes for different iron-containing activators. As can be seen in Figure 2g and 2h, the FeCl_3 -sample has a remarkably similar particle surface, morphology and porous structure to the starting biomass. SEM micrographs of the graphitized coffee grounds without iron activator are shown in Figure S1. In contrast, SEM images of the other samples (Figure 2a–f) reveal a flake-shaped morphology composed of agglomerates of graphite plates. In particular, for the Fe-sample, some particles showed a perfectly spherical morphology that resembles that of commercial SG materials and were not found for the other samples (Figure S2). One should note that Fe_2O_3 and Fe activator particles have initial sizes of $<1\ \mu\text{m}$ and $<5\ \mu\text{m}$ (Figure S3), respectively. Those particle sizes are expected to be significantly larger than those resulting from the decomposition of FeCl_3 and $\text{Fe}(\text{NO}_3)_3$ and might have an influence on the graphitization mechanism.^[29]

Structural characteristics of carbon materials

The structural properties as well as the DoG of carbonaceous samples were first examined *via* Raman spectroscopy due to its sensitivity towards structural disorder.^[30] Characteristic Raman

signals for carbons originate from various lattice vibrations from the graphene layers. Only one first-ordered band (G-band) would occur for perfectly stacked graphene layers at a Raman shift of $1580\ \text{cm}^{-1}$.^[31] It can be attributed to the in-plane stretching motion of the C=C double bond with E_{2g} -symmetry.^[30] Theoretically, there are four additional first-ordered defect bands (D bands) occurring in graphitic carbons and carbonaceous materials stemming from structural disorder.^[30] The most distinct defect band is the D1 mode observed at $\approx 1350\ \text{cm}^{-1}$, caused by lattice vibrations with A_{1g} -symmetry mainly at the edges of graphene layers in amorphous carbon. Also, the presence of heteroatoms within the structure could lead to the occurrence of the D1 band.^[32] A further band commonly observed is the D2 band at $\approx 1620\ \text{cm}^{-1}$ as a shoulder of the G band. It only occurs at graphene layers, which are not sandwiched by other layers.^[32a,33] D3 and D4 defect bands are primarily observed for highly amorphous carbonaceous materials at $1500\ \text{cm}^{-1}$ and $1200\ \text{cm}^{-1}$ due to the sp^2 - sp^3 bonds of C–C and C=C stretching vibrations of polyene-like structures, respectively.^[32a] An additional peak appears at $\approx 2700\ \text{cm}^{-1}$, which is the second order of the D band (2D) and is influenced by the order of stacking in *c*-direction.

The measured Raman spectra of carbonaceous materials exhibit all five D bands as well as the G band (Figure 3). Overall, the D1 band intensity decreases proportionally to the G band from FeCl_3 to Fe-powder (top to bottom, Figure 3-a). The intensity ratio between G and D1 bands (I_{D1}/I_G) is often used as an indicator of the extent of graphitization in carbonaceous samples.^[32a] However, the values obtained using the integrated peak area intensities of the G and D1 bands are only an

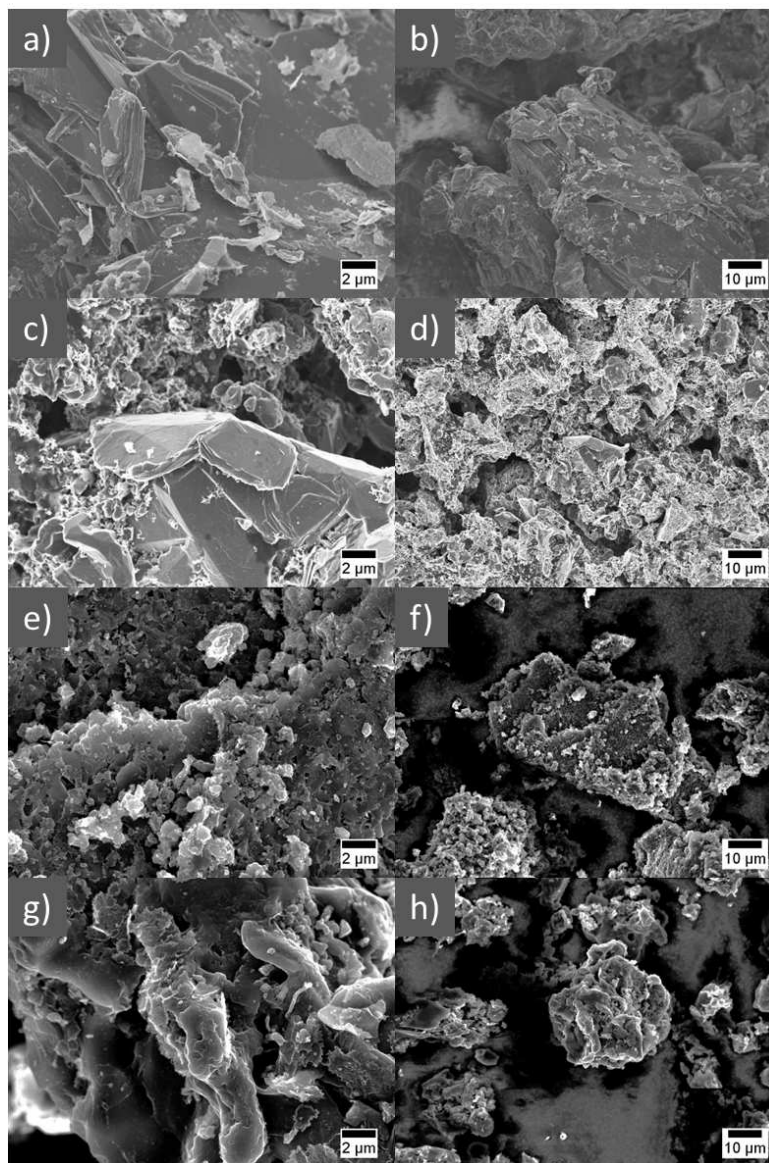


Figure 2. SEM micrographs of coffee-ground derived carbons at 2000 °C using a, b) Fe, c, d) Fe₂O₃, e, f) Fe(NO₃)₃ and g, h) FeCl₃ as activators.

estimation and should be interpreted with caution. A more accurate statement can be achieved by fitting G, D1, D2 and D4 bands with Lorentzian functions and the D3 band with a Gaussian function according to *Sadezky et al.*^[32a] Figure 3-b shows an example of fitted spectrum for FeCl₃-derived carbonaceous material. Detailed Raman fitting results and contributions of the different modes for all samples can be seen in Figure S4 and Table S2. The highest I_{D1}/I_G-ratio of 0.82 is obtained by the volatile activator FeCl₃. The I_{D1}/I_G-ratio decreases to 0.49, 0.45, 0.36 when using Fe(NO₃)₃, Fe₂O₃ and Fe, respectively (Figure S5a). Therefore, the sample synthesized using Fe-powder as activator has the highest development of the graphitic structure among all measured samples. The DoG (0 ≤ DoG ≤ 1) and the crystallite size in a-direction (L_a) can be calculated by the integrated intensity ratios of D1 and G bands according to the following equations (Eqs. 1 and 2):^[34]

$$\text{DoG} = \frac{I_G}{I_{D1} + I_G} \quad (1)$$

$$L_a = 2.4 \cdot 10^{-10} \cdot \lambda^4 \left(\frac{I_{D1}}{I_G} \right)^{-1} \quad (2)$$

After fitting the Raman data as shown in Figure 3c, a decreasing DoG regarding the activator as follows was found: Fe (74%) > Fe₂O₃ (69%) > Fe(NO₃)₃ (67%) > FeCl₃ (55%). The highest DoG is thus achieved by using Fe as activator in the graphitization process, while the lowest value of 55% was obtained by the volatile activator FeCl₃, as expected from our previous results and the estimated values based on the I_{D1}/I_G-ratio.^[22a] The value reported here is a bit lower than that reported in our previous study for FeCl₃ (DoG of ≈ 69%). However, in that study only different spots within one particle were measured and might not be representative of the whole

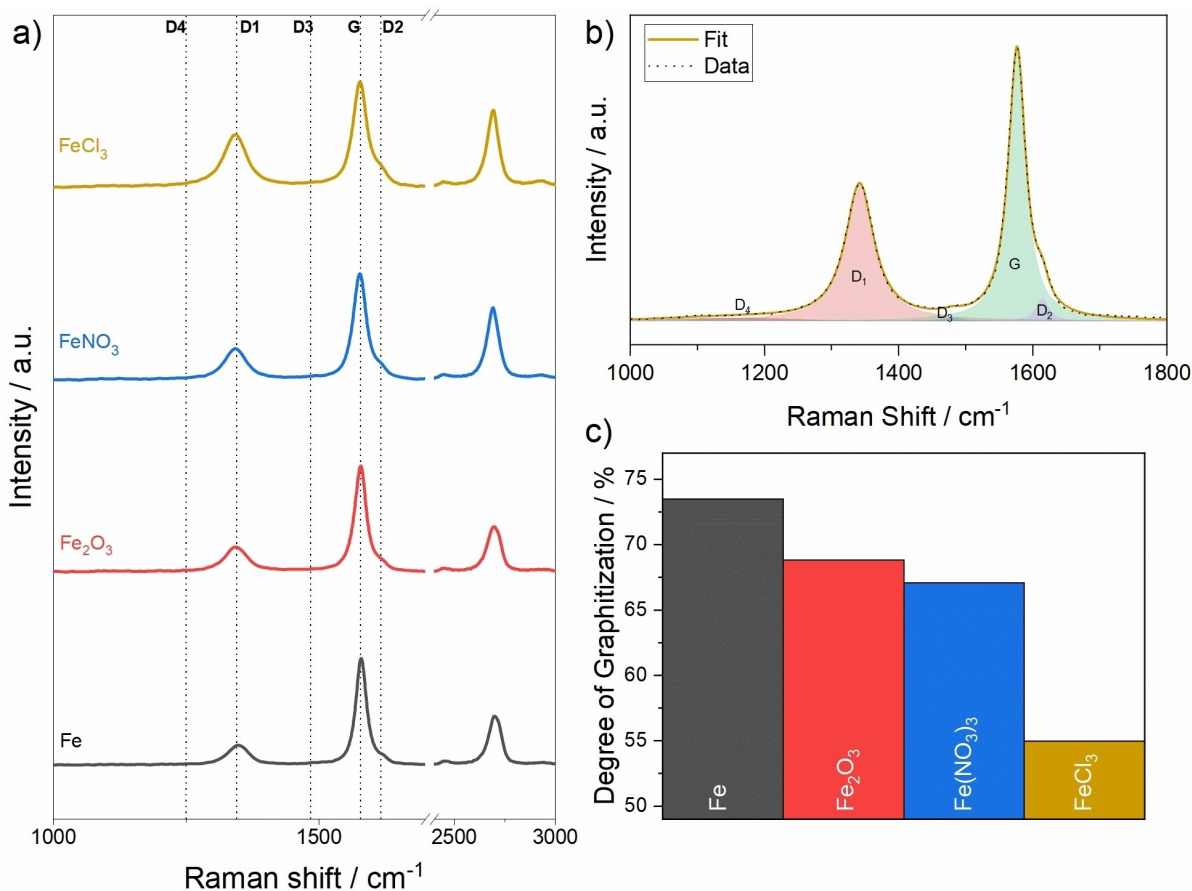


Figure 3. a) Raman spectra of synthesized carbonaceous materials with different activators, b) fitting of Raman spectrum to determine the DoG (example for FeCl₃-derived sample), c) calculated DoG values for each activator-derived carbonaceous material.

sample. Interestingly, the DoG values of Fe₂O₃ and Fe(NO₃)₃-derived carbonaceous materials are quite similar to each other. This could be explained by hydrolysis of Fe(NO₃)₃ after addition of the solvent to Fe₂O₃. It might be that still some Fe(NO₃)₃ residues are left in the sample which explains the slightly different DoG.

Furthermore, the relative peak area of the D₂-band at ≈ 1620 cm⁻¹ can be used to get information about the stacking mechanism of carbonaceous materials. The relative D₂ peak area decreases from 3.0% to 0.8% from FeCl₃ to Fe-powder (Figure S5b), indicating the higher extent of stacking of the Fe-derived materials. Moreover the difference between Fe₂O₃ and Fe(NO₃)₃ is higher than for Fe and Fe₂O₃ (Table S2) indicating the physical mixing being more beneficial towards the graphitization of carbonaceous materials. Similarly, the crystallite size in the a-direction (Figure S5c), L_a , was calculated to be ≈ 23.5 nm (FeCl₃), 39.2 nm (Fe(NO₃)₃), 42.4 nm (Fe₂O₃) and 53.3 nm (Fe). Furthermore, I_{D2}/I_G as well as I_{D2}/I_{D1} ratios were calculated to get an idea of the degree of stacking of graphene sheets.^[20b] However, no clear trend that would be helpful to understand the effect of different activators was found (Table S2). The I_{D2}/I_G ratio seems to decrease for samples with a higher DoG (i.e., Fe and Fe₂O₃ following a dry mixing approach). According to these results, a simple physical mixing/addition of

the activator (Fe) seems to have a more positive impact on the 'catalytic' graphitization mechanism, which we further investigated by X-ray diffraction measurements as well as electrochemical analysis.

To gain further insights into the local ordering of the partially-graphitized samples synthesized at 2000 °C using different iron-based activators, total scattering X-ray diffraction experiments were performed in MSPD beamline of the ALBA synchrotron. Figure 4 shows the normalized and corrected scattering factor, which is proportional to the diffracted intensity. There are slight differences between carbonaceous samples, especially with regards to the sharpening of diffraction reflections. The atomic pair distribution function (PDF) has emerged as a powerful tool for the study of hard carbon or partially graphitized materials with limited long-range ordering.^[18,35] The PDF contains information regarding the interatomic distances in a material and was extracted from the scattered data according to the following equation (Eq. 3):

$$G(r) = \frac{2}{\pi} \int_0^{\infty} Q[S(Q) - 1] \sin(Qr) dQ \approx \frac{2}{\pi} \int_{Q_{\min}}^{Q_{\max}} Q[S(Q) - 1] \sin(Qr) dQ \quad (3)$$

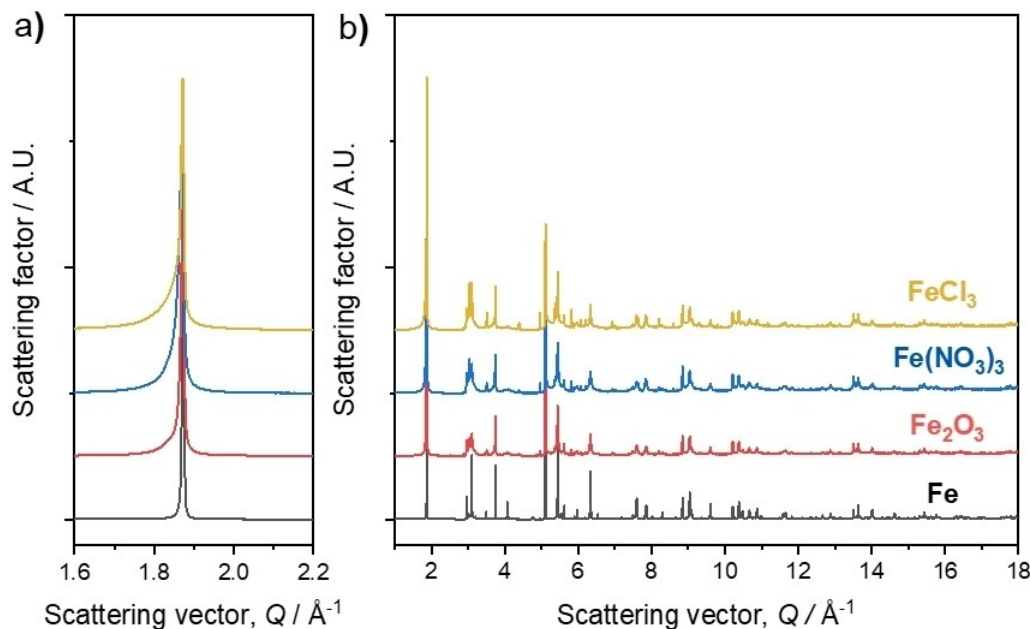


Figure 4. Normalized scattering factor for the coffee ground-derived carbonaceous samples. Left graph shows a magnified view of the (002) reflection in graphite.

with Q being the modulus of the scattering vector, and r the interatomic distance separating pair of atoms.

The so-called small-box model using the crystalline structure of graphite was considered as a starting point to refine PDF data and obtain structural parameters, as previously reported to study hard carbons.^[18,36] For this approach, a crystalline structure containing the basic short-range atomic unit (hexagonal carbon rings in this case) was initially considered and the long-range order was smoothed by introducing long-range disorder.^[36] The disorder was introduced through anisotropic atomic displacement parameters (ADPs), which are allowed to take unphysical values describing static disorder. Lattice parameters a and c , anisotropic displacement parameters U_{11} , average coherent crystalline distance or crystallite size, and a global scale factor were refined in the r range 0.5–20 Å. U_{11} was set equal to U_{22} to maintain the in-plane symmetry of graphene layers in the graphitic structure.

The observed and calculated PDFs from the refined structural model are shown in Figure 5a for all samples. As can be seen, this is a one-dimensional function which oscillates around zero and shows peaks centered on the average r interatomic distances separating pair of atoms, related to the increase of the local atomic density to the average value. For small interatomic distances, the PDF shows peaks at atom-atom distances well matching those in a basic graphene unit, while the lack of long-range ordering manifests as a decaying amplitude of the PDF with increasing atomic distance r .

Detailed information of refinements, lattice parameters and ADPs can be found in Table S3. Agreement factors R_{wp} were generally below 30% suggesting that the refinements are reliable and there is a good agreement between measured and calculated data.^[19] The lattice parameter a (Figure 5b), which is

related to the average in-plane interatomic distances in the structural graphene unit, remained constant and very similar to that of graphite ($a = 2.461$ Å). The interlayer distances ($c/2$) are slightly higher than in ideal graphite ($c = 3.35$ Å) and range between 3.35 and 3.38 Å (Figure 5c), corresponding to the Fe and FeCl_3 samples, respectively. A higher interlayer or interplanar spacing between graphene sheets can be ascribed to the presence of less-ordered turbostratic regions. U_{11} and U_{33} are indicative of in-plane and out-of-plane disorder in the graphitic structure, respectively. While U_{11} remains almost constant at $\approx 2 \times 10^{-3}$ Å², a value that is physically compatible with thermal motion, the out-of-plane atomic displacement parameter U_{33} follows the same trend as the interplanar distance (Figure 5d). The sample synthesized with FeCl_3 as iron-source shows the highest value (≈ 0.05 Å²) due to its higher disorder. The estimated crystallite size (Figure 5e) shows the following descending order for the investigated iron-based activators: $\text{Fe} > \text{Fe}_2\text{O}_3 > \text{Fe}(\text{NO}_3)_3 > \text{FeCl}_3$, in agreement with the DoG estimated from Raman results.

Dry mixing vs. wet-mixing approach using different activators

Findings from SEM, Raman and PDF results indicate intriguing differences between samples. The carbonaceous sample prepared using Fe-powder showed a significant better development of the graphitic structure. The coherent crystallite size, or more specifically the coherent crystalline distance, is significantly larger (≈ 115 Å) compared to the other samples. In contrast, the sample using FeCl_3 showed a limited long-range structural order which can stem from the volatility of the precursor itself.^[24] According to previous works,^[29] the micro-

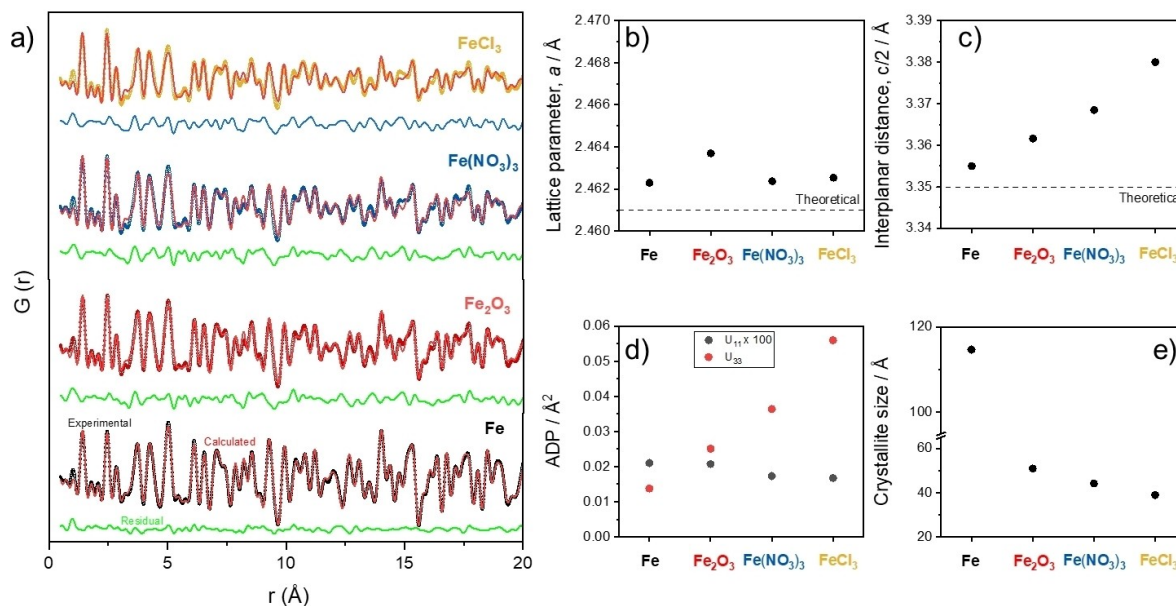


Figure 5. Results obtained from the fitting of the PDFs to a disordered graphite structure: a) Observed (coloured hollow circles) and calculated (red lines) values of the PDF, along with the difference curves (green ones). b) Lattice parameter a , c) interplanar spacing ($c/2$), d) in-plane (U_{11}) and out-of-plane (U_{33}) ADPs, and e) average crystallite size. U_{11} is multiplied by a factor of 100.

structure of the resulting graphitic samples might not only intimately be linked to the carbonization temperature, additive concentration, and impregnation method^[19a,23b,24,37] but also to the additive particle size. Even though samples wet-impregnated with Fe(NO₃)₃ and FeCl₃ in an organic-based solution are expected to have a more homogenous dispersion of the additive and a better contact with the biomass-derived carbon, they unexpectedly show lower DoG values which might stem from a different reaction mechanism.^[22a] According to some of the earliest works on catalytic graphitization by Oya et al. using Ni as additive, if the particles were finely divided in the order of a few nanometers in size (e.g., ≈ 20 nm) onion-like graphitic layers surrounding catalyst particles were precipitated.^[29] However, larger particles formed by coarsening upon heating led to the precipitation of three-dimensional bulk graphite crystals. This effect was also observed in previous studies using FeCl₃ at temperatures ranging between 1000 and 2000 °C by high-resolution transmission electron microscopy (TEM).^[19a,23b]

Two reaction mechanisms have been proposed in literature for 'catalytic' graphitization of carbon/iron mixtures, i.e., dissolution-precipitation at temperatures higher than the melting point of pure iron (~ 1540 °C)^[38] and carbide formation/decomposition at much lower temperatures.^[39] In the case of wet-impregnation with FeCl₃ and Fe(NO₃)₃, the iron salt precursor is decomposed upon heat treatment resulting in the formation of iron oxide nanoparticles before forming a carbide that later decomposes into metallic iron and additional graphite from low temperatures below 1000 °C.^[19f] Conversely, for the dry mixing approach using Fe powder with a relatively large particle size, a dissolution-precipitation mechanism within molten iron 'catalyst' particles might be responsible for the formation of three-dimensional graphite platelets.^[39c] Li et al.^[40] reported the onset of graphitization to occur at ~ 1200 °C when

mixing powders of milled coke carbon and Fe (particle sizes < 74 and < 5 μm , respectively). It might be expected that large particle sizes of Fe in that study probably limited the formation of iron carbide (Fe₃C) due to the sluggish diffusion kinetics, and thus, graphitization only started when a liquid phase formed *via* a solution/re-precipitation mechanism. However, the (002) reflection of graphite is present in all our samples at 1000 °C (Figure S6) regardless of the initial iron-based precursor. The absence of iron carbide (Fe₃C) reflections in the XRD pattern of Fe and Fe₂O₃ samples (Figure S6) might indicate that the most dominant graphitization mechanism for these samples is the dissolution-precipitation mechanism. Nevertheless, future studies with precise control of the additive particle size are needed to investigate the actual impact on the DoG.

Electrochemical performance in carbon || Li metal cells

The impact of the development of graphitic structures, observed by both Raman spectroscopy and XRD, on the electrochemical performance was investigated by constant current cycling (CCC) experiments in carbon || Li metal cells (half-cell setup using a three-electrode cell configuration with lithium metal as counter (CE) and reference electrodes (RE)).^[41] The rate-capability investigations, to check the fundamental properties of the materials, at rates between 0.1 C and 10 C (1 C equals to 372 mA g⁻¹) are shown in Figure 6a.

The maximum specific de-lithiation capacities attained follow the same trend as the DoG and crystallite size estimated by Raman analysis and PDF results: Fe > Fe₂O₃ > Fe(NO₃)₃ > FeCl₃. During the whole rate capability experiment, Fe-derived carbonaceous material exhibits outstanding performance and the highest capacities with little deviation at even high rates of

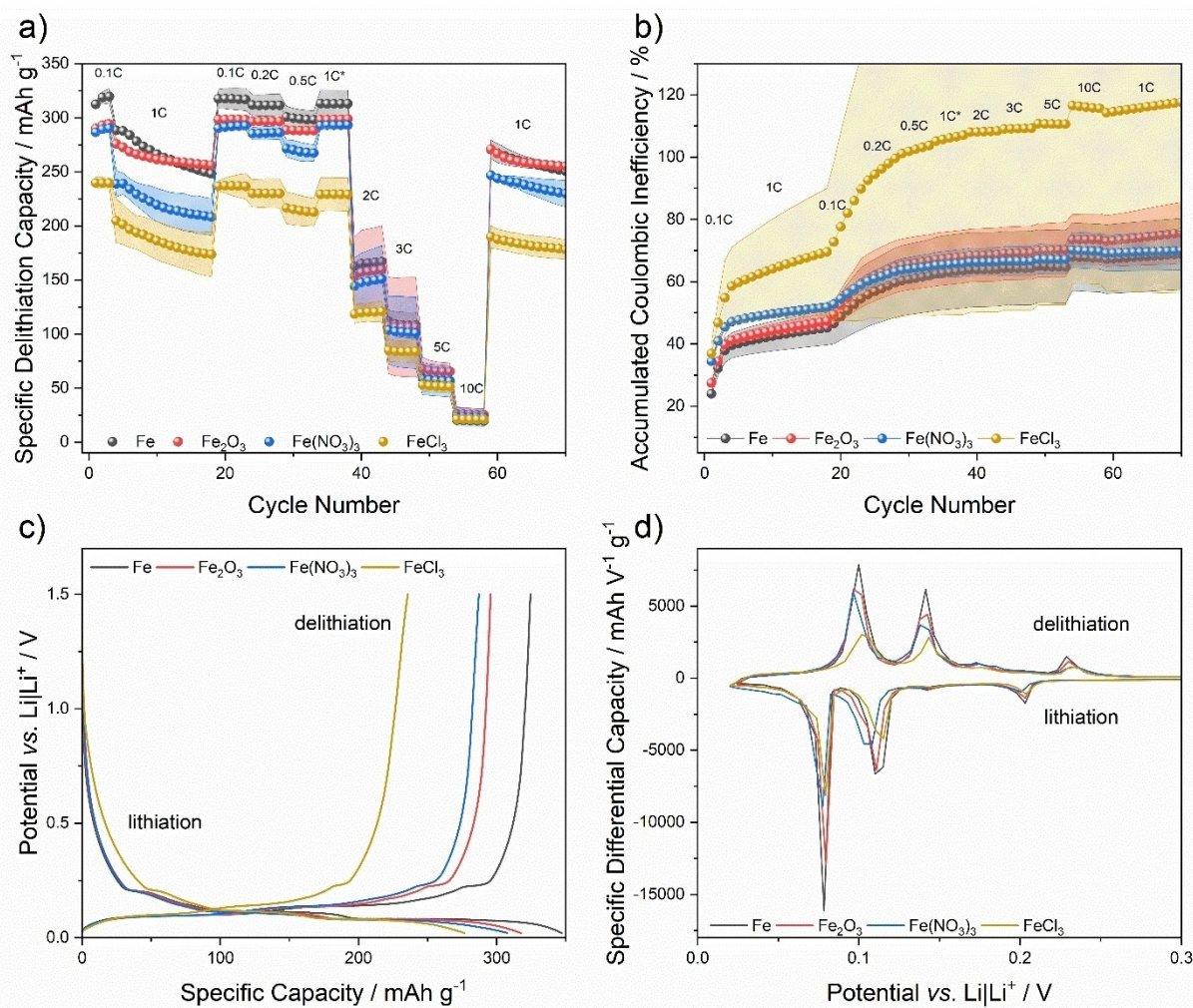


Figure 6. a) Charge/discharge rate performance studies and b) accumulated Coulombic efficiencies at rates between 0.1 and 10 C of carbon || Li metal cells for carbonaceous materials synthesized at 2000 °C. c) 1st cycle potential profiles and d) differential capacity (dQ/dV) vs. potential profiles of carbon || Li metal cells (three-electrode configuration, half-cell setup with Li metal as CE and RE). Electrolyte: 1 M LiPF₆ in EC/EMC (3:7) + 2 wt% VC; potential range: 0.02 to 1.5 V vs. Li | Li⁺.

5 C and 10 C. During (de-)lithiation at high C-rates, the capacities significantly fade due to slower lithiation kinetics due to hindrance of Li⁺ ion intercalation into the graphite layered structures compared to the adsorption/insertion of Li⁺ ions into hard carbon structures.^[42] This capacity drop becomes more evident for the more graphitic samples (i.e., Fe, Fe(NO₃)₃ and Fe₂O₃). Once the rate returns back to 1 C (after 59 cycles), the delithiation capacities are nearly maintained or increased compared to the capacities at the beginning of the C-rate experiments, reflecting good electrochemical reversibility.

Initial Coulombic efficiencies (C_{eff}) of $\approx 63\%$ (FeCl₃), 66% (Fe(NO₃)₃), 72% (Fe₂O₃) and 76% (Fe) were achieved and differences can be due to solid electrolyte interphase (SEI) formation in the first cycle. In order to present the evolution of the C_{eff} upon cycling more qualitatively, accumulated Coulombic inefficiencies (ACI) were plotted in Figure 6b. ACI can reflect parasitic reactions within the LIB cell, including but not limited to reductive electrolyte decomposition and loss of active lithium for interphase formation (SEI^[43],^[44]). As can be seen, all

cells show a similar increase of ACI except for FeCl₃-derived materials which exhibit a steady increase, which can be caused by distinct active lithium loss or more severe electrolyte degradation. This can be most likely related to the more amorphous character, and thus higher porosity and higher amount of surface groups in that sample.^[42]

According to the 1st cycle potential profiles and specific differential capacity (dQ/dV) vs. potential plots in Figure 6c–d, the highly graphitic character of the materials can be reflected in the characteristic peaks of staging phenomena of Li⁺ ion intercalation into graphite at potentials < 0.2 V vs. Li | Li⁺.^[45] By further examination of the potential profiles, the ascending trend regarding the DoG is also supported by increasing peak intensities, i.e., the highest intensity is achieved for the Fe-carbonaceous sample and the lowest for FeCl₃. Also the quite similar capacity for both Fe₂O₃ and Fe(NO₃)₃ derived carbonaceous materials supports the above mentioned positive effect of undissolved addition of the activator due to hydrolysis of

$\text{Fe}(\text{NO}_3)_3$ to Fe_2O_3 resembling a 'quasi *in-situ*' physical addition process.

To better elucidate the effect of different iron sources on the electrochemical performance, Figure 7 shows the 1st cycle C_{Eff} as well as specific delithiation capacities of coffee ground-derived carbons at 0.1 C (averaged specific delithiation capacities of first three cycles) as a function of the DoG estimated from Raman measurements and the crystallite size estimated from PDF measurements. There seems to be a strong dependence between both structural parameters and the electrochemical results. As can be seen, maximum reversible capacities of $\approx 240 \text{ mAhg}^{-1}$ (FeCl_3), 290 mAhg^{-1} ($\text{Fe}(\text{NO}_3)_3$), 294 mAhg^{-1} (Fe_2O_3), 320 mAhg^{-1} (Fe) were achieved at a rate of 0.1 C. Therefore, the higher the DoG and crystallite size, the higher the achievable capacity and C_{Eff} in the first cycle. Moreover, the more graphitic character of some samples result in lower non-basal surfaces, as seen by SEM analysis, that might help with the formation of a more effective SEI, less active lithium losses and thus higher C_{Eff} values in the first cycles.^[46]

Although the electrochemical performance of Fe-derived materials is superior to that of other samples and to even that of petroleum-coke derived carbons reported in previous works using similar experimental conditions for cell testing,^[45c] it is important to note that initial C_{Eff} values and initial capacities achieved herein are lower than those of commercial graphites.^[4b,19c] The theoretical specific capacity of graphite is 372 mAhg^{-1} and values about $350\text{--}360 \text{ mAhg}^{-1}$ are often achieved for commercial SG anodes. To meet the requirements for industrial application it is mandatory to achieve $>99.9\%$ C_{Eff} within the first few cycles. Furthermore, the materials need purities $>99.95\%$, high crystallinity, appropriate cycle as well as calendar life and a fitting morphology. Further particle sizing and shaping, surface refinements or carbon coating approaches typically done in graphite anode material production industrially could also be performed to improve such values. However, further modification steps are beyond the goal of this work and can only be performed in kg-scale.^[1b] The goal of this work was rather to provide a systematic study on the effect of different iron-based precursors on the graphitization efficiency. Future

works will focus not only on further material optimization but also on recycling of the used iron-based activator during the synthesis which could be used in further 'catalytic graphitization' processes.

When comparing the results reported here with previous literature (Table S4), Banek et al. investigated hardwood sawdust using 62.5 wt% of Fe-powder as activator resulting in a maximum capacity of 358 mAhg^{-1} .^[25a] Gomez-Martin et al. also investigated 'catalytic graphitization' behavior of wood-based biomass precursors using FeCl_3 as activator. Reversible capacities of 307 mAhg^{-1} were achieved at 2000°C using $\sim 35 \text{ wt}\%$ FeCl_3 .^[19a] Our previous results from Hanhart et al. showed a saturation point regarding both, achievable DoGs and reversible capacities, between 40 and 50 wt% when using FeCl_3 as activator.^[22a] After graphitization at 2000°C , a specific delithiation capacity of 243 mAhg^{-1} was reached from coffee ground with FeCl_3 which is $\sim 60 \text{ mAhg}^{-1}$ less than wood-based materials. Comparing results from coffee ground treated with Fe-powder to Banek's wood materials, a difference of only 41 mAhg^{-1} in capacity is observed, also supporting the higher impact of Fe-powder regarding the graphitizing mechanism than volatile activators such as FeCl_3 . However, the highest achieved specific delithiation capacity here of 320 mAhg^{-1} is already close to capacities often achieved by commercial graphites, and might be increased by further optimization.^[47]

In light of these results, one should keep in mind that parameters such as starting biomass material and synthesis procedure itself (e.g., conventional heat-treatment vs. laser pyrolysis) differ for various reports and those differences can directly impact the graphitization behavior and might not be directly compared. However, our results suggest that it is worth further investigating the role of Fe-powder content to reveal whether there is also a saturation point in the degree of crystallinity and whether the particle size of the activator has also a key role on the graphitization.^[25a]

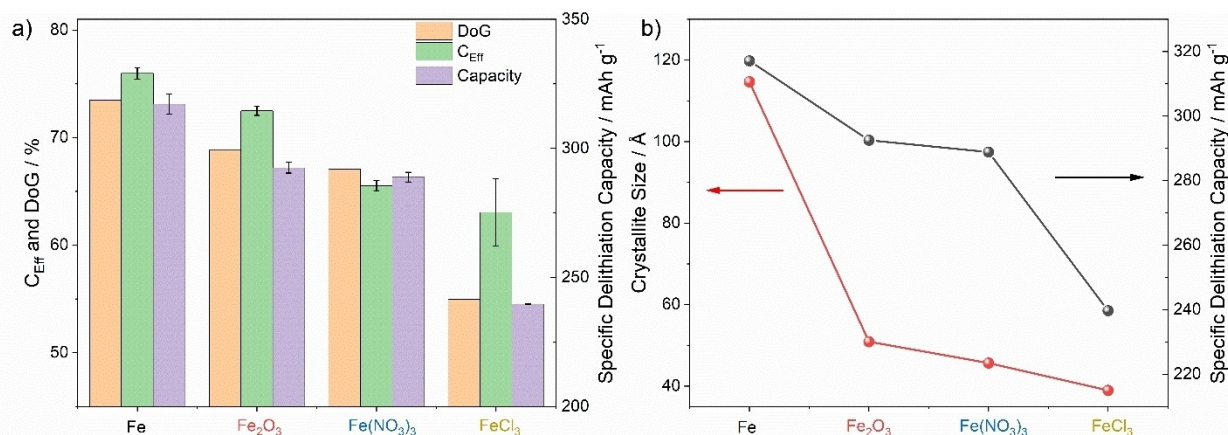


Figure 7. a) Averaged specific delithiation capacity of first three cycles and 1st cycle C_{Eff} as a function of the DoG and iron-based activator. b) Averaged specific delithiation capacity as a function of crystallite size as estimated from PDF results.

Conclusions

Four different iron-based activators were systematically investigated revealing their impact on the so-called 'catalytic graphitization' behavior of coffee ground at 2000 °C regarding structural evolution as well as electrochemical performance in carbon || Li metal cells. Previous studies on the volatile activator FeCl₃ revealed optimized temperature region as well as activator content beyond which there is a saturation point in the degree of graphitization. Raman and total scattering X-ray along with PDF results here reveal a critical impact of the additive on the structural parameters and extent of graphitization. A maximum DoG of 74% and longer range-order was obtained by using micron-sized Fe powder as activator by simple physical mixing approach. It seems more beneficial not only towards the mechanism but also to reduce preparation time which takes several hours to days for wet chemical impregnation method using FeCl₃ and Fe(NO₃)₃. Specific delithiation capacities of up to 320 mAhg⁻¹ were achieved using Fe powder. The results of this study can pave the way for the synthesis of outstanding 'green' anode materials which can compete with commercial SG obtained by non-sustainable sources. However, electrochemical properties are still far from meeting commercial requirements. Specific delithiation capacities and first cycle C_{Eff} values are lower than those of well-manufactured natural or synthetic graphites for LIBs. The latter might strongly prevent the direct application in full-cells due to the possible consumption of active lithium from the cathode. These parameters can be further improved by optimized graphitization conditions and particle refinements.

In summary, this work reveals a significant impact of the impregnation method and possibly also of the particle size on the 'catalytic graphitization' process. Future studies will investigate the impact of iron particle size, lowest possible activator concentration to achieve sufficiently high DoGs, suitable particle treatments to improve C_{Eff} and recycling of the used activator. Moreover, the way of addition of activator should be more deeply investigated to understand the impact of its homogeneity during heat treatment.

Experimental

Synthesis of carbonaceous materials

Coffee ground (*Caffè Crema Classico, Lavazza, Italy*) was used as biomass precursor material for the synthesis of (graphitic) carbonaceous materials. Four different iron-based precursors were investigated: iron (III) chloride hexahydrate (FeCl₃·6H₂O; *Emsure*, purity: 99%), iron (III) nitrate nonahydrate (Fe(NO₃)₃·9H₂O; *Sigma-Aldrich*, purity: 98%), iron (III) oxide (Fe₂O₃, *Alfa Aesar*, purity: 99%) and iron (Fe; *Sigma-Aldrich*, purity: 99%) powders. SEM images of starting Fe₂O₃ and Fe powders are shown in Figure S3.

First, to introduce the iron-based activator before the carbonization process, the dried precursor was impregnated with a solution of the iron-based salts (FeCl₃·6H₂O or Fe(NO₃)₃·9H₂O) in acetone for 12 hours. Fe₂O₃ and Fe powders were physically mixed with the coffee ground using a planetary centrifugal mixer (Thinky Mixer ARE-310, *THINKY U.S.A., INC*) for 4 minutes to provide an overall

homogeneous distribution. For a fair comparison of the investigated iron salts, a Fe:C mass ratio of 1:1 (50 wt%) was used for all samples. The carbon yield after the carbonization of the biomass precursor was determined by thermogravimetric analysis up to 1000 °C under argon atmosphere. The mixture was then heat-treated in a RS80/750/13 oven (*Nabertherm GmbH*) according to the following procedure: 1 °C min⁻¹ up to 500 °C, held for one hour before heating up to 1000 °C for three hours with a temperature ramp rate of 5 °C min⁻¹. A constant argon flow of 66 Lh⁻¹ was used.

After carbonization, the impregnated coffee ground-derived carbons were heat-treated again in a *LHTG 200-300/30-2G*-oven (*Carbolite Gero GmbH & Co.KG*) for graphitization. A maximum temperature of 2000 °C was reached using a heating rate of 200 °C h⁻¹ under argon atmosphere (500 Lh⁻¹). The maximum temperature was held for 10 hours.

Finally, the carbonaceous materials were stirred in concentrated HNO₃ (> 69%; *Sigma-Aldrich*) overnight to remove the remaining activator. All samples were rinsed with deionized water until a neutral pH-value was reached and dried in a *Binder (Binder GmbH)* oven at 80 °C. All powder samples were sieved to a grain size below 45 μm for electrode preparation.

Characterization of carbonaceous materials

Total scattering experiments were performed at Material Science Powder Diffraction (MSPD) beamline of the ALBA-CELLS synchrotron. Beam energy was 30 keV (wavelength λ = 0.4133 Å as confirmed using a Si standard) and scattering was measured up to 2θ = 120° using an array of position-sensitive detectors (*Dectris Mythen*), resulting in a usable scattering vector range of Q ~ 0.5–25 Å⁻¹. The measurement time was 45 min per sample. Powdered carbon samples free of residual iron were contained in 0.7 mm polyimide tubes. The background scattering signal of an empty tube was subtracted from the data. The pair distribution function (PDF) of each sample was calculated by Fourier transforming the coherently scattered signal using an *ad hoc* polynomial correction as implemented in PDFGetX3 software.^[48] Further analysis of the obtained PDFs was performed using PDFGui.^[49]

To determine the DoG of the samples with respect to the iron-based precursor, Raman spectroscopy was performed using a Bruker Senterra Raman microscope (*Bruker Optics Inc.*) with a green semiconductor laser, operating at a wavelength of 532 nm with a power of 5 mW. A 1024×256 pixel charge-coupled device (CCD) detector was used, which is cooled down thermoelectrically to -65 °C. The carbonaceous materials were focused using a microscope with a 50× magnification objective. Five different spots from different particles per sample were measured, performing ten co-additions with an integration time of 60 s for each spectrum. Raman spectra were deconvoluted using in-house written code implemented in MATLAB and a non-linear least-squares fitting using pseudo-Voigt line-shape functions.

Scanning electron microscopy (SEM) analyses were carried out using a *Carl Zeiss AURIGA* scanning electron microscope (*Carl Zeiss Microscopy GmbH*) to evaluate the particle morphology of carbon materials. The typical accelerating voltage was 3 kV.

ICP-OES measurements were conducted to determine the mass fraction of iron after carbonization. Measurements were performed using an *ARCOS (Spectro Analytical Instruments GmbH)* with an axial positioned plasma torch. All other parameters were applied according to Vortmann and Evertz et al.^[50] Nitrogen adsorption measurements were carried out on a *3Flex (Micromeritics Instrument Corporation)* by use of liquid nitrogen at its boiling temperature of -196 °C. All samples were degassed prior measurements at 250 °C

under reduced pressure (< 0.05 mbar) for at least 12 h. The specific surface area and structural properties were calculated by the Brunauer–Emmett–Teller (BET) theory and density functional theory (DFT) based on the experimental data.

All samples were structurally characterized before iron removal by powder X-ray diffraction (PXRD) measurements after carbonization at 1000°C using a Bruker D8 Advanced X-ray powder diffractometer (Bruker AXS GmbH) applying a nickel filtered copper K_α -radiation ($\lambda = 0.154$ nm; 40 kV and 40 mA) in the range of $2\theta = 10^\circ$ – 90° with a step size of 0.021° . To correct instrumental contributions, the samples were mixed with 10 wt% of sieved pure silicon (Si) powder, which was used as internal standard.

Electrode preparation, cell assembly and electrochemical characterization

Composite electrodes with a composition of 94 wt% carbonaceous active material, 2 wt% conductive agent (Super C65, Imerys Graphite & Carbon), 2 wt% styrene-butadiene rubber (SBR, LIPATON SB 5521, Synthomer) and 2 wt% sodium-carboxymethyl cellulose (Na-CMC, Walocel CRT 2000 PPA 12, Dow Wolff Cellulosics) as binder materials. First, SBR and Na-CMC binders were stirred in deionized water using a magnetic bar. After complete dispersion, conductive agent as well as the carbonaceous material were added. After addition of each component, the mixture was stirred at 10,000 rpm for one hour for complete homogenization by using a Dispermat LC30 (Motor type 5BCu2-042, VMA-Getzmann GmbH). The resulting electrode paste was coated onto dendritic copper foil (Schlenk Metallfolien GmbH & Co. KG) using standard doctor-blade technique with a ZUA 2000 Universal Applicator (ZEHNTER GmbH) to ensure the desired coating height and an Automatic Film Applicator 1133 N (Sheen Instruments) with a speed of 50 mm s^{-1} . After coating, the electrode sheets were dried in a laboratory oven (Binder GmbH) at 80°C for 1 hour and electrode discs ($\varnothing = 12$ mm) were punched afterwards using a Hohsen electrode puncher (Hohsen Corp.). Punched electrodes were further dried in a Büchi Glass Oven B-585 (Büchi) at 120°C for 12 hours under reduced pressure (≤ 0.05 mbar) to remove residual water. Afterwards, the electrodes were weighed using a Sartorius ME 235S analytical balance (Sartorius AG) with an accuracy of ± 0.01 mg and stored at room temperature in a dry room (dew point of at least -50°C , 0.02% moisture content).

Electrochemical evaluation of carbonaceous electrodes was performed in carbon || Li metal Swagelok T-cells with a three-electrode configuration (half-cell set-up).^[41] The synthesized carbonaceous material electrodes were used as working electrode (WE; $\varnothing = 12$ mm). Lithium metal discs (Albemarle Corporation) were used as counter (CE, $\varnothing = 12$ mm), as well as reference electrodes (RE, $\varnothing = 5$ mm). The cell body was electronically isolated by using Mylar foils (polyethylene terephthalate (PET)). 1 M LiPF_6 in a mixture of ethylene carbonate (EC) and ethyl methyl carbonate (EMC) in a ratio of 3:7 by weight (Solvionic; purity: battery grade) with 2 wt% of the film-forming additive vinylene carbonate (VC) served as electrolyte. Freudenberg FS2190 polyolefin separators were placed between WE and CE ($\varnothing = 13$ mm, 6-layered, soaked with $120\ \mu\text{L}$ electrolyte) as well as in the RE ($\varnothing = 8$ mm, 3-layered, soaked with $80\ \mu\text{L}$ electrolyte). Three cells from each carbon sample were evaluated to ensure the reproducibility of the results. The standard deviation of each three cells is represented with the help of error bars in the corresponding figures. Electrodes with an active mass loading of 2.5 ± 0.1 mg ($\approx 2.2\text{ mg cm}^{-2}$) were used for electrochemical investigations.

The electrochemical investigations were carried out on a Maccor Series 4000 automated test system (Maccor Inc.) at room temperature. The current rate (C-rate) performance of the synthesized

materials was investigated in carbon || Li metal cells via constant current charge/discharge cycling (CCC) at different specific currents in the potential range between 0.02 and 1.5 V vs. Li | Li⁺ (half-cell setup). The specific current for a rate of 1 C was defined as 372 mA g^{-1} based on the theoretical capacity of graphite (372 mAh g^{-1}). The cycling procedure was as follows: first, after initial resting for six hours, three formation cycles at 37.2 mA g^{-1} are followed by 15 cycles at 372 mA g^{-1} which is then followed by each 5 cycles at 37.2 mA g^{-1} , 74.4 mA g^{-1} , 186 mA g^{-1} , 372 mA g^{-1} (after 38 cycles a constant voltage step was applied at a potential of 20 mV vs. Li | Li⁺; current limitation: 18.6 mA g^{-1} , 744 mA g^{-1} , 1116 mA g^{-1} , 1860 mA g^{-1} and 3720 mA g^{-1} and after that additional 12 cycles at 372 mA g^{-1} .

Supporting Information

Supporting Information is available from the Wiley Online Library or from the author.

Acknowledgements

Author from the University of Münster thank the Ministry of Economic Affairs, Innovation, Digitalization and Energy of the State of North Rhine-Westphalia (MWIDE) for funding this work in the project 'GrEEn' (313-W044A). High energy X-ray diffraction and Pair Distribution Function measurements were performed at the Materials Science and Powder Diffraction (BL04-MSPD) beamline at ALBA Synchrotron with the collaboration of ALBA staff. We are grateful to Dr. Aleksandr Missiul for his assistance during these experiments. Joaquin Ramirez-Rico acknowledges financial support from Junta de Andalucía under Grants no. P20-01186 (PAIDI 2020) and US-1380856 (FEDER Andalucía 2014-20), as well as Spanish Ministry of Science and Innovation under Grant no. PID2019-107019RB-I00 (co-financed with FEDER funds). The authors thank Verena Naber for performing ICP-OES measurements. Open Access funding enabled and organized by Projekt DEAL.

Conflict of Interest

The authors declare no conflict of interest.

Data Availability Statement

The data that support the findings of this study are available from the corresponding author upon reasonable request.

Keywords: activator · anode material · carbonization · 'catalytic' graphitization · lithium ion batteries

[1] a) M. Winter, B. Barnett, K. Xu, *Chem. Rev.* **2018**, *118*, 11433–11456; b) R. Schmuch, R. Wagner, G. Hörpel, T. Placke, M. Winter, *Nat. Energy* **2018**, *3*, 267–278.

- [2] J. Betz, G. Bieker, P. Meister, T. Placke, M. Winter, R. Schmich, *Adv. Energy Mater.* **2019**, *9*, 1803170.
- [3] S. Dühnen, J. Betz, M. Kolek, R. Schmich, M. Winter, T. Placke, *Small Methods* **2020**, *4*, 2000039.
- [4] a) M. Armand, P. Axmann, D. Bresser, M. Copley, K. Edström, C. Ekberg, D. Guyomard, B. Lestriez, P. Novák, M. Petranikova, W. Porcher, S. Trabesinger, M. Wohlfahrt-Mehrens, H. Zhang, *J. Power Sources* **2020**, *479*, 228708; b) P. Meister, H. Jia, J. Li, R. Kloepsch, M. Winter, T. Placke, *Chem. Mater.* **2016**, *28*, 7203–7217.
- [5] a) T. Placke, G. G. Eshetu, M. Winter, E. Figgemeier, in *Lithium-ion Batteries Enabled by Silicon Anodes* (Eds.: C. Ban, K. Xu), The Institution of Engineering and Technology (IET), **2021**, pp. 349–404; b) Y. An, Y. Tian, H. Wei, B. Xi, S. Xiong, J. Feng, Y. Qian, *Adv. Funct. Mater.* **2020**, *30*, 1908721.
- [6] a) G. G. Eshetu, E. Figgemeier, *ChemSusChem* **2019**, *12*, 2515–2539; b) M. N. Obrovac, *Curr. Opin. Electrochem.* **2018**, *9*, 8–17; c) S. Chae, M. Ko, K. Kim, K. Ahn, J. Cho, *Joule* **2017**, *1*, 47–60.
- [7] a) C. Heubner, T. Liebmann, O. Lohrberg, S. Cangaz, S. Maletti, A. Michaelis, *Batteries & Supercaps* **2022**, *5*, e202100182; b) M. Abdollahifar, A. Vinograd, C.-Y. Lu, S.-J. Chang, J. Müller, L. Frankenstein, T. Placke, A. Kwade, M. Winter, C.-Y. Chao, N.-L. Wu, *ACS Appl. Mater. Interfaces* **2022**, *14*, 38824–38834.
- [8] a) J. Asenbauer, T. Eisenmann, M. Kuenzel, A. Kazzazi, Z. Chen, D. Bresser, *Sustain. Energy Fuels* **2020**, *4*, 5387–5416; b) F. Duffner, N. Kronmeyer, J. Tübke, J. Leker, M. Winter, R. Schmich, *Nat. Energy* **2021**, *6*, 123–134.
- [9] J. Clark, *Webinar – 7th December 2020, Benchmark Mineral Intelligence* **2020**.
- [10] P. Dolega, M. Buchert, J. Betz, *Short study prepared within the framework of the BMBF joint project Fab4Lib, Oeko-Institut*, <https://www.oeko.de/en/publications/p-details/environmental-and-socio-economic-challenges-in-battery-supply-chains-graphite-and-lithium>, **2020**.
- [11] a) *European Commission*, <https://ec.europa.eu/docsroom/documents/27348/attachments/1/translations/en/renditions/pdf> **2018**; b) P. Dolega, W. Bulach, J. Betz, S. Degreif, M. Buchert, *Policy Brief, Oeko-Institut e.V.* **2021**; c) *U. S. Department of the Interior, U. S. Geological Survey*, <https://www.usgs.gov/publications/mineral-commodity-summaries-2022>, **2022**.
- [12] a) M. Wissler, *J. Power Sources* **2006**, *156*, 142–150; b) H. Jäger, W. Frohs, M. Banek, M. Christ, J. Daimer, F. Fendt, C. Friedrich, F. Gojny, F. Hiltmann, R. Meyer zu Reckendorf, J. Montminy, H. Ostermann, N. Müller, K. Wimmer, F. von Sturm, E. Wege, K. Roussel, W. Handl, in *Ullmann's Encyclopedia of Industrial Chemistry*, Wiley-VCH Verlag GmbH & Co. KGaA, **2000**; c) S. M. Lee, D. S. Kang, J. S. Roh, *Carbon Lett.* **2015**, *16*, 135–146.
- [13] G. Juri, H. A. Wilhelm, J. L'Heureux, *CFI Ceram. Forum Int.* **2007**, *84*, E22–E25.
- [14] W. Lämmerer, H. Flachberger, *BHM Berg- Huettenmaenn. Monatsh. Suppl.* **2017**, *162*, 336–344.
- [15] a) W.-J. Liu, H. Jiang, H.-Q. Yu, *Energy Environ. Sci.* **2019**, *12*, 1751–1779; b) C. Liedel, *ChemSusChem* **2020**, *13*, 2110–2141; c) N. Soltani, A. Bahrami, L. Giebler, T. Gemming, D. Mikhailova, *Prog. Energy Combust. Sci.* **2021**, *87*, 100929; d) Y. Feng, L. Tao, Z. Zheng, H. Huang, F. Lin, *Energy Storage Mater.* **2020**, *31*, 274–309.
- [16] a) Y. Sun, X.-L. Shi, Y.-L. Yang, G. Suo, L. Zhang, S. Lu, Z.-G. Chen, *Adv. Funct. Mater.* **2022**, *32*, 2201584; b) D. Saurel, B. Orayech, B. Xiao, D. Carriazo, X. Li, T. Rojo, *Adv. Energy Mater.* **2018**, *8*, 1703268.
- [17] a) P. Ouzilleau, A. E. Gheribi, P. Chartrand, G. Soucy, M. Monthieux, *Carbon* **2019**, *149*, 419–435; b) M. Winter, K.-C. Moeller, J. O. Besenhard, in *Lithium Batteries: Science and Technology* (Eds.: G.-A. Nazri, G. Pistoia), Springer US, Boston, MA, **2003**, pp. 145–194.
- [18] A. Gomez-Martin, J. Martinez-Fernandez, M. Ruttter, M. Winter, T. Placke, J. Ramirez-Rico, *Chem. Mater.* **2019**, *31*, 7288–7299.
- [19] a) A. Gomez-Martin, J. Martinez-Fernandez, M. Ruttter, A. Heckmann, M. Winter, T. Placke, J. Ramirez-Rico, *ChemSusChem* **2018**, *11*, 2776–2787; b) Q. Yan, J. Li, X. Zhang, E. B. Hassan, C. Wang, J. Zhang, Z. Cai, *J. Nanopart. Res.* **2018**, *20*, 223; c) A. Gomez-Martin, J. Martinez-Fernandez, M. Ruttter, M. Winter, T. Placke, J. Ramirez-Rico, *ACS Omega* **2019**, *4*, 21446–21458; d) A. Oya, H. Marsh, *J. Mater. Sci.* **1982**, *17*, 309–322; e) Y. C. Liu, Q. L. Liu, J. J. Gu, D. M. Kang, F. Y. Zhou, W. Zhang, Y. Wu, D. Zhang, *Carbon* **2013**, *64*, 132–140; f) A. Gomez-Martin, Z. Schnepf, J. Ramirez-Rico, *Chem. Mater.* **2021**, *33*, 3087–3097; g) R. Hunter, J. Rowlandson, G. J. Smales, B. R. Pauw, V. Ting, A. N. Kulak, Z. Schnepf, *Mater. Adv.* **2020**, *1*, 3281–3291.
- [20] a) M. P. Illa, C. S. Sharma, M. Khandelwal, *Mater. Today Chem.* **2021**, *20*, 100439; b) M. M. Gaikwad, C. S. Sharma, *J. Mater. Res.* **2020**, *35*, 2989–3003; c) M. Kakunuri, S. Kali, C. S. Sharma, *J. Anal. Appl. Pyrolysis* **2016**, *117*, 317–324.
- [21] a) F. J. Maldonado-Hódar, C. Moreno-Castilla, J. Rivera-Utrilla, Y. Hanzawa, Y. Yamada, *Langmuir* **2000**, *16*, 4367–4373; b) C. J. Thambiliyagadage, S. Ulrich, P. T. Araujo, M. G. Bakker, *Carbon* **2018**, *134*, 452–463.
- [22] a) V. Hanhart, L. Frankenstein, J. Ramirez-Rico, V. Siozios, M. Winter, A. Gómez Martín, T. Placke, *ChemElectroChem* **2022**, *9*, e202200819; b) E. Thompson, A. E. Danks, L. Bourgeois, Z. Schnepf, *Green Chem.* **2015**, *17*, 551–556; c) C. S. Bitencourt, A. P. Luz, C. Pagliosa, V. C. Pandolfelli, *Ceram. Int.* **2015**, *41*, 13320–13330; d) Q. Yan, J. Li, X. Zhang, J. Zhang, Z. Cai, *Nanomater. Nanotechnol.* **2018**, *8*; e) S. Kubo, Y. Uraki, Y. Sano, *J. Wood Sci.* **2003**, *49*, 188–192.
- [23] a) Y. Liu, Q. Liu, J. Gu, D. Kang, F. Zhou, W. Zhang, Y. Wu, D. Zhang, *Carbon* **2013**, *64*, 132–140; b) A. Gutiérrez-Pardo, J. Ramirez-Rico, R. Cabezas-Rodríguez, J. Martínez-Fernández, *J. Power Sources* **2015**, *278*, 18–26.
- [24] J. Hoekstra, A. M. Beale, F. Soulimani, M. Versluijs-Helder, D. van de Kleut, J. M. Koelewijn, J. W. Geus, L. W. Jenneskens, *Carbon* **2016**, *107*, 248–260.
- [25] a) N. A. Banek, K. R. McKenzie, D. T. Abele, M. J. Wagner, *Sci. Rep.* **2022**, *12*, 8080; b) N. A. Banek, D. T. Abele, K. R. McKenzie, M. J. Wagner, *ACS Sustainable Chem. Eng.* **2018**, *6*, 13199–13207.
- [26] S. Bundesamt, Import von Kaffee nach Deutschland von September 2020 bis September 2022 (in Tonnen), <https://de.statista.com/statistik/daten/studie/12497/umfrage/kaffee-importmenge-nach-deutschland-pro-monat/>, accessed.
- [27] A. Bengtsson, J. Bengtsson, M. Sedin, E. Sjöholm, *ACS Sustainable Chem. Eng.* **2019**, *7*, 8440–8448.
- [28] C. Wang, R. Zou, M. Qian, X. Kong, E. Huo, X. Lin, L. Wang, X. Zhang, R. Ruan, H. Lei, *Bioresour. Technol.* **2022**, *355*, 127251.
- [29] A. Öya, S. Ötani, *Carbon* **1981**, *19*, 391–400.
- [30] A. C. Ferrari, J. Robertson, *Phys. Rev. B* **2000**, *61*, 14095–14107.
- [31] F. Tuinstra, J. L. Koenig, *J. Chem. Phys.* **1970**, *53*, 1126–1130.
- [32] a) A. Sadezky, H. Muckenhuber, H. Grothe, R. Niessner, U. Pöschl, *Carbon* **2005**, *43*, 1731–1742; b) G. Katagiri, H. Ishida, A. Ishitani, *Carbon* **1988**, *26*, 565–571.
- [33] M. A. Pimenta, G. Dresselhaus, M. S. Dresselhaus, L. G. Cançado, A. Jorio, R. Saito, *Phys. Chem. Chem. Phys.* **2007**, *9*, 1276–1290.
- [34] a) L. G. Cançado, K. Takai, T. Enoki, M. Endo, Y. A. Kim, H. Mizusaki, A. Jorio, L. N. Coelho, R. Magalhães-Paniago, M. A. Pimenta, *Appl. Phys. Lett.* **2006**, *88*, 163106; b) J. Ramirez-Rico, A. Gutierrez-Pardo, J. Martinez-Fernandez, V. V. Popov, T. S. Orlova, *Mater. Des.* **2016**, *99*, 528–534.
- [35] a) S. J. L. Billinge, M. G. Kanatzidis, *Chem. Commun.* **2004**, 749–760; b) R. E. Franklin, *Proc. Roy. Soc. A* **1951**, *209*, 196–218; c) R. E. Franklin, *Acta Crystallogr.* **1950**, *3*, 107–121.
- [36] V. Petkov, R. G. Difrancesco, S. J. L. Billinge, M. Acharya, H. C. Foley, *Philos. Mag. B* **1999**, *79*, 1519–1530.
- [37] a) R. Othman, A. S. Kamal, N. H. Jabarullah, *Prod. Eng. Arch.* **2021**, *27*, 124–129; b) J. Hoekstra, A. M. Beale, F. Soulimani, M. Versluijs-Helder, J. W. Geus, L. W. Jenneskens, *J. Phys. Chem. C* **2015**, *119*, 10653–10661.
- [38] S. Liu, C. R. Loper, *Carbon* **1991**, *29*, 547–555.
- [39] a) O. P. Krivoruchko, V. I. Zaikovskii, *Mendeleev Commun.* **1998**, *8*, 97–99; b) S. Glatzel, Z. Schnepf, C. Giordano, *Angew. Chem. Int. Ed.* **2013**, *52*, 2355–2358; *Angew. Chem.* **2013**, *125*, 2411–2414; c) R. D. Hunter, J. Ramirez-Rico, Z. Schnepf, *J. Mater. Chem. A* **2022**, *10*, 4489–4516.
- [40] H. Li, H. Zhang, K. Li, J. Zhang, M. Sun, B. Su, *Fuel* **2020**, *279*, 118531.
- [41] R. Nölle, K. Beltrop, F. Holtstiege, J. Kasnatscheew, T. Placke, M. Winter, *Mater. Today* **2020**, *32*, 131–146.
- [42] a) S. R. Sivakkumar, J. Y. Nerkar, A. G. Pandolfo, *Electrochim. Acta* **2010**, *55*, 3330–3335; b) M. Winter, J. O. Besenhard, *Handbook of Battery Materials* (Eds.: C. Daniel, J. O. Besenhard) **2011**, Second Edition, 433–478.
- [43] D. R. Gallus, R. Wagner, S. Wiemers-Meyer, M. Winter, I. Cekic-Laskovic, *Electrochim. Acta* **2015**, *184*, 410–416.
- [44] F. Holtstiege, A. Wilken, M. Winter, T. Placke, *Phys. Chem. Chem. Phys.* **2017**, *19*, 25905–25918.
- [45] a) M. S. Dresselhaus, G. Dresselhaus, *Adv. Phys.* **1981**, *30*, 139–326; b) A. Missyul, I. Bolshakov, R. Shpanchenko, *Powder Diffr.* **2017**, *32*, S56–S62; c) O. Fromm, A. Heckmann, U. C. Rodehorst, J. Frerichs, D. Becker, M. Winter, T. Placke, *Carbon* **2018**, *128*, 147–163; d) A. Gomez-Martin, J. Martinez-Fernandez, M. Ruttter, A. Heckmann, M. Winter, T. Placke, J. Ramirez-Rico, *ChemSusChem* **2018**, *11*, 2776–2787.
- [46] a) K. Persson, V. A. Sethuraman, L. J. Hardwick, Y. Hinuma, Y. S. Meng, A. van der Ven, V. Srinivasan, R. Kostecki, G. Ceder, *J. Phys. Chem. Lett.* **2010**, *1*, 1176–1180; b) T. Placke, V. Siozios, R. Schmitz, S. F. Lux, P. Bieker, C. Colle, H. W. Meyer, S. Passerini, M. Winter, *J. Power Sources*

- 2012, 200, 83–91; c) T. Placke, V. Siozios, S. Rothermel, P. Meister, C. Colle, M. Winter, in *Z. Phys. Chem.*, Vol. 229, 2015, pp. 1451–1469.
- [47] M. Endo, C. Kim, K. Nishimura, T. Fujino, K. Miyashita, *Carbon* 2000, 38, 183–197.
- [48] P. Juhás, T. Davis, C. Farrow, S. Billinge, *J. Appl. Crystallogr.* 2013, 46, 560–566.
- [49] C. L. Farrow, P. Juhas, J. W. Liu, D. Bryndin, E. S. Božin, J. Bloch, T. Proffen, S. J. L. Billinge, *J. Phys. Condens. Matter* 2007, 19, 335219.
- [50] a) M. Evertz, J. Kasnatscheew, M. Winter, S. Nowak, *Anal. Bioanal. Chem.* 2019, 411, 277–285; b) B. Vortmann-Westhoven, M. Winter, S. Nowak, *J. Power Sources* 2017, 346, 63–70.

Manuscript received: October 28, 2022
Revised manuscript received: November 28, 2022
Version of record online: January 13, 2023